

# Direct measurement of neutrons induced in lead by cosmic muons at a shallow underground site

Q. Du<sup>a,b,\*</sup>, I. Abt<sup>b</sup>, A. Empl<sup>b,c</sup>, C. Gooch<sup>b</sup>, R. Kneissl<sup>b</sup>, S.T. Lin<sup>a</sup>, B. Majorovits<sup>b</sup>, M. Palermo<sup>b,d</sup>, O. Schulz<sup>b</sup>, L. Wang<sup>e</sup>,  
Q. Yue<sup>e</sup>, A.J. Zsigmond<sup>b</sup>

<sup>a</sup>College of Physical Science and Technology, Sichuan University, Chengdu 610064, China

<sup>b</sup>Max Planck Institute for Physics, Munich 80805, Germany

<sup>c</sup>Department of Physics, University of Houston, Houston 77204, USA

<sup>d</sup>now at Physics and Astronomy Department, University of Hawaii, Honolulu 96822, USA

<sup>e</sup>Department of Engineering Physics, Tsinghua University, Beijing 100084, China

---

## Abstract

Neutron production in lead by cosmic muons has been studied with a Gadolinium doped liquid scintillator detector. The detector was installed next to the Muon-Induced Neutron Indirect Detection EXperiment (MINIDEX), permanently located in the Tübingen shallow underground laboratory where the mean muon energy is approximately 7 GeV. The MINIDEX plastic scintillators were used to tag muons; the neutrons were detected through neutron capture and neutron-induced nuclear recoil signals in the liquid scintillator detector. Results on the rates of observed neutron captures and nuclear recoils are presented and compared to predictions from GEANT4-9.6 and GEANT4-10.3. The predicted rates are significantly too low for both versions of GEANT4. For neutron capture events, the observation exceeds the predictions by factors of  $1.65 \pm 0.02(\text{stat.}) \pm 0.07(\text{syst.})$  and  $2.58 \pm 0.03(\text{stat.}) \pm 0.11(\text{syst.})$  for GEANT4-9.6 and GEANT4-10.3, respectively. For neutron nuclear recoil events, which require neutron energies above approximately 5 MeV, the factors are even larger,  $2.22 \pm 0.05(\text{stat.}) \pm 0.25(\text{syst.})$  and  $3.76 \pm 0.09(\text{stat.}) \pm 0.41(\text{syst.})$ , respectively. Also presented is the first statistically significant measurement of the spectrum of neutrons induced by cosmic muons in lead between 5 and 40 MeV. It was obtained by unfolding the nuclear recoil spectrum. The observed neutron spectrum is harder than predicted by GEANT4. An investigation of the distribution of the time difference between muon tags and nuclear recoil signals confirms the validity of the unfolding procedure and shows that GEANT4 cannot properly describe the time distribution of nuclear recoil events. In general, the description of the data is worse for GEANT4-10.3 than for GEANT4-9.6.

**Keywords:** Neutrons induced by cosmic muons, Neutron spectrum, Lead, Liquid scintillator

---



---

\*Corresponding author: qiang.du@stu.scu.edu.cn

## 1. Introduction

Muon-induced neutrons are an important background for underground experiments searching for rare events such as neutrinoless double beta decays [1, 2], direct dark matter interactions [3, 2] or neutrino interactions in oscillations experiments [4, 2]. Experiments can sufficiently shield against neutrons from the radio-impurities in the rock surrounding the laboratories, because the kinetic energy of these neutrons is usually below 10 MeV and, thus, they are efficiently thermalized by low Z materials such as water or polyethylene. It is more difficult to shield against neutrons induced by cosmic muons because the high-energy muons that penetrate deep into the ground can produce neutrons with much higher energies.

A particular case are experiments using high-Z materials like lead, steel and copper for shields [5] close to the active detector. The cross sections for muons to generate neutrons in these materials are large and the neutrons can reach kinetic energies up to several GeV. These high energy neutrons have a large penetration power and can create secondary showers with many neutrons reaching the vicinity of the active detectors. In addition, the active detector itself can be made out of a high-Z material, like in the case of Germanium based experiments to search for neutrinoless double beta decay [1, 5] or dark matter [6]. The experiments usually have a muon veto, which is used to reject signals following the passage of a muon. However, the neutrons from the showers can create meta-stable states in the inner structures or active parts of an experiment which can decay minutes or hours later and cannot be vetoed easily. An example is the creation of  $^{77m}\text{Ge}$  from  $^{76}\text{Ge}$ , for which the decay scheme includes a beta decay with a half-life of 12 hours [7].

There are four main processes how muons generate neutrons inside matter:

- muon-nuclear deep inelastic scattering;
- photo-nuclear reactions, i.e. Bremsstrahlung photons induce photo-disintegration;
- hadronic inelastic scattering, i.e. muon-induced secondary hadrons cause hadron-induced spallation;
- $\mu^-$  capture, i.e. nuclei excited by  $\mu^-$  capture release neutrons.

Muon capture is only relevant in shallow underground sites with a depth of  $\lesssim 100$  m water equivalent (*mwe*) [8].

The production of muon-induced neutrons has been investigated for different materials and at different depths for many years [9]. In this paper, the focus is on lead as a target material. Details about some selected experiments on lead are listed in Table 1.

Of the experiments previous to this work listed in Table 1, only the experiment at the Holborn underground laboratory [15] has published a measurement of the spectrum of the neutrons induced by cosmic muons, albeit with low statistical significance. In addition, the target was composed of a mixture of lead and rock and no corresponding simulation was available. Complementary to the underground experiments on neutrons induced by cosmic muons, two accelerator based experiments measured muon-induced neutron

Table 1: Underground experiments on neutrons induced by cosmic muons in lead

Depth [mwe]	Lead thick- ness [cm]	Reference
12	15	G. V. Gorshkov(1974)[10]
16	50	I. Abt (2017)[11] and this work
20	7.6	M. F. Crouch (1952)[12][13]
40	10	G. V. Gorshkov (1971)[14]
58	— <sup>a</sup>	Holborn (1965)[15]
60	10	L. Bergamasco (1970)[16]
80	10	G. V. Gorshkov (1971)[14]
110	10	L. Bergamasco (1970)[16]
150	10, 16	Gorshkov (1968[17], 1971[18])
800	10	G. V. Gorshkov (1971)[14]
2850	— <sup>b</sup>	Boulby (2008[8], 2013[19])
4300	35	L. Bergamasco (1973)[20]
4800	10	LSM (2013)[9]

<sup>a</sup> The lead was mixed with rock and the neutron spectrum was measured with low statistical significance.

<sup>b</sup> The target was the whole lead shielding system of the ZEPLIN-II and ZEPLIN-III experiments.

spectra in lead. These were the E665 experiment at Fermilab using a 470 GeV muon beam [21] and the NA55 experiment at CERN using a 190 GeV muon beam [22]. The results of the NA55 experiment were compared to GEANT4-8.0 simulations and significant discrepancies in neutron multiplicities and angular distributions were found [23]. An updated experiment using a 160 GeV muon beam has recently been performed [24].

In this paper, a detailed investigation of neutrons induced by cosmic muons in lead is presented. The experiment was performed in the shallow underground laboratory at the University of Tübingen. Thus, the results cannot be directly used to predict the background in deep underground laboratories. They can, however, be used to evaluate the Monte Carlo (MC) programs used to make such predictions.

To measure the spectrum of muon-induced neutrons, a 28-liter Gadolinium doped (0.5% in weight) liquid scintillator (Gd-LS) detector was installed next to the MINIDEX (Muon-Induced Neutron Indirect Detection EXperiment) [11] setup. The details of the experimental setup and the detector concept are introduced in Section 2. The energy calibration is described in Section 3. The selections of events and their processing are presented in Section 4. The details of the MC simulations are described in Section 5. The results are given in Section 6. A discussion on the MC performance and a summary are presented in the last two Sections.

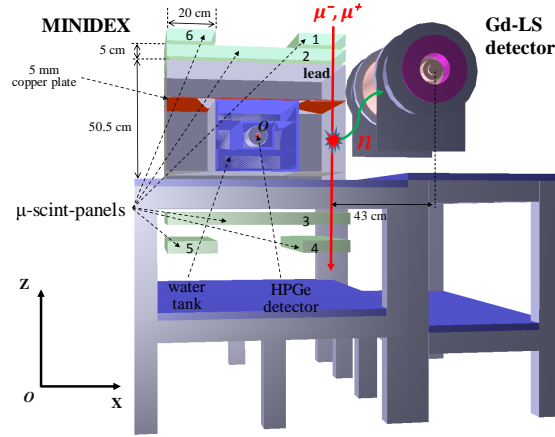


Fig. 1: The MINIDEX setup together with the Gadolinium doped liquid scintillator (Gd-LS) detector. The six muon scintillator panels ( $\mu$ -scint-panels) were used to independently identify cosmic muons passing through the left-side and right-side lead walls. Signals in the four muon scintillator panels labeled 1, 2, 3 and 4 were required to select muon-induced signals in the Gd-LS detector. A steel box enclosing the Gd-LS detector is not shown.

## 2. Experimental setup and detector concept

The Gd-LS detector was placed next to one of the lead walls of the MINIDEX in the underground laboratory in Tübingen. The nominal vertical depth of the site was given [25] as 16 *mwe*; the cover consists predominantly of soil. According to simulation, which is described in Section 5, the average energy of the cosmic muons entering the laboratory was  $\approx 7 \text{ GeV}$ <sup>1</sup>. The geometry of the MINIDEX setup plus the Gd-LS detector is shown in Fig. 1. A detailed description of MINIDEX is given in [11]. Here, only components relevant for the analysis of the data from the Gd-LS detector data are described.

In the standard MINIDEX analysis, neutrons were identified with two high-purity germanium (HPGe) detectors embedded in a water tank. These were used to detect 2.2 MeV  $\gamma$ -rays emitted after neutron capture in water. The dimensions of the water tank were  $35 \times 55 \times 30 \text{ cm}^3$  with a  $15 \times 55 \times 10 \text{ cm}^3$  central cavity in which the HPGe detectors were inserted. The water tank and the HPGe detectors were fully surrounded by a lead castle, used both as a shield for the HPGe detectors and as the target for muons to generate neutrons. The thickness of the lead castle was 15 cm at the top supported by a 5 mm thick copper plate, 5 cm at the bottom and 5 cm for the two side walls at right angle to the HPGe and Gd-LS detectors which are not shown in Fig. 1. The two lead walls parallel to the Gd-LS detectors were 20 cm thick. These two walls are hereafter referred to as the left-side and right-side lead walls where the right-side wall is next to the Gd-LS detector.

<sup>1</sup>The technical drawings and the result of the simulation indicate that the value of 16 *mwe* is an overestimate and that the overburden more closely corresponds to 12 *mwe*, see also Section 5.

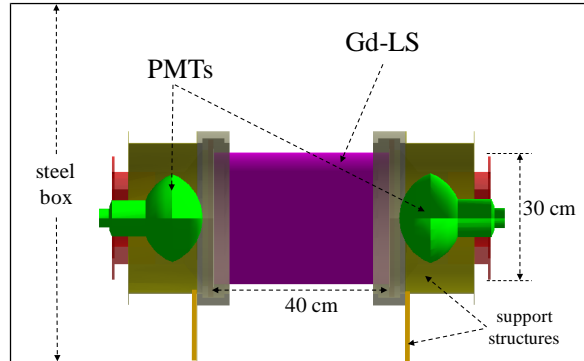


Fig. 2: Schematic of the Gd-LS detector. The Gd-LS type EJ-335 was contained in a 8 mm thick tempered borosilicate glass cylinder with a diameter of 30 cm diameter and a length of 40 cm. Two 8-inch photomultiplier tubes (PMTs) were connected to the two flat end-surfaces of the glass cylinder with light guides. The active detector was located inside a light-tight steel box.

A schematic of the Gd-LS detector is shown in Fig. 2. Organic liquid scintillator (EJ-335) was held inside a 8 mm thick tempered borosilicate glass cylinder with a diameter of 30 cm and a length of 40 cm. The EJ-335 was produced by the Eljen Technology company and was loaded with 0.5% Gadolinium by weight [26]. Two 8-inch photomultiplier tubes (PMTs) were connected to the two flat end-plates of the glass cylinder with light guides. The active detector was protected inside a light-tight steel box. The distance between the center of the Gd-LS detector and the center of the right-side lead wall was 43 cm.

Data was taken together with MINIDEX from January to July 2016. The data acquisition was run without trigger, i.e. the data stream from all components was recorded continuously. The association of neutron signals to muons was done offline with the plastic scintillator panels of MINIDEX being used as a muon tagger. The dimensions of the muon scintillator panels were  $75 \times 65 \times 5 \text{ cm}^3$  for the two big panels (2 and 3 in Fig. 1) and  $20 \times 65 \times 5 \text{ cm}^3$  for the four small panels (1, 4, 5 and 6 in Fig. 1). The two big panels fully covered the top and the bottom of the lead castle. For the analysis presented here, only muons passing through the full lengths (50 cm) of the lead wall next to the Gd-LS detector were considered. They were identified by coincidences of signals in the four panels 1, 2, 3 and 4; this will be described in detail in Section 4.1.

Figure 3 illustrates the detection of neutrons, which were created by cosmic muons in the lead, in the Gd-LS detector. If a muon passage through the right-side lead wall was tagged, following neutron signals were searched for. Neutrons created in the lead by muons directly or in a muon-induced shower at time  $t_\mu$  had a finite probability to propagate into the Gd-LS detector. The range of typical times of flight  $\Delta t_{n-\mu}$  is tens to hundreds of nanoseconds. Neutrons with a sufficiently high energy will first create a signal from a prompt nuclear recoil at time  $t_n$  through (multiple) elastic scattering on the nuclei of the liquid scintillator (proton or carbon). Then, after thermalization, neutrons will diffuse for a few microseconds ( $\sim 7 \mu\text{s}$ ) until

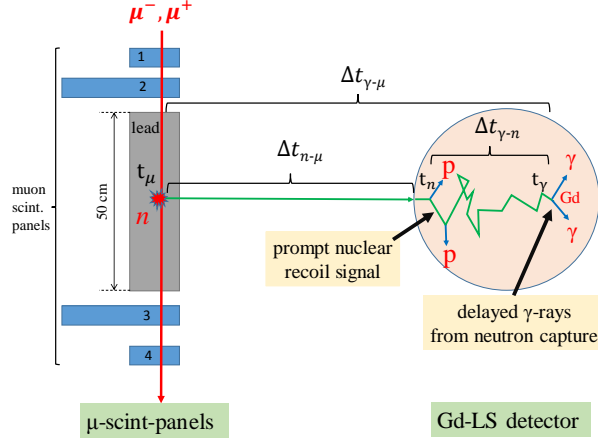


Fig. 3: The principle of detecting muon-induced neutrons in the Gd-LS detector.

they are captured by Gd. A neutron capture is followed by a rapid ( $< \text{ns}$ ) release of several  $\gamma$ -rays with a total energy of around 8 MeV at time  $t_\gamma$ . This results in a  $\gamma$ -signal delayed with respect to the nuclear recoil signal by  $\Delta t_{\gamma-n}$  and to the muon signal by  $\Delta t_{\gamma-\mu}$ .

The unique combination of the muon signal, the prompt nuclear recoil signal and the delayed  $\gamma$ -signal, as well as the characteristic times  $\Delta t_{n-\mu}$ ,  $\Delta t_{\gamma-n}$  and  $\Delta t_{\gamma-\mu}$  provide a highly background suppressed measurement of neutrons induced in lead by muons. In most muon-induced neutron experiments, the detectors are located below or above the targets. In this case, the Gd-LS detector was placed at the side of the target which is of great advantage as the detection of the neutrons was not disturbed by the muons producing them.

### 3. Energy calibration and threshold

The energy calibration of the Gd-LS detector was performed using the detector response to a variety of  $\gamma$  rays and to minimum ionizing cosmic muons (m.i.p.s.). The gamma rays originated from  $\gamma$  lines of a  $^{60}\text{Co}$  and a  $^{228}\text{Th}$  source, the 2.2 MeV  $\gamma$ -line from de-excitation after neutron capture in hydrogen and the 4.438 MeV  $\gamma$ -line from an AmBe neutron source.

The response of the detector to  $\gamma$  rays from the calibration sources and muons was simulated by implementing the detector setup in GEANT4 [27]. The energy resolution of the detector was limited and had to be determined together with the energy scale. It was modeled as a Gaussian  $\sigma = \sqrt{a \cdot E}$  [28] with a variable parameter  $a$  to be adjusted. The resolution parameter  $a$  was determined to be 30 keV by matching the observed and simulated widths of the peaks. The visible line energies were also fitted. Due to the limited resolution they are shifted downwards from the nominal  $\gamma$  line energies because part of the Compton shoulders could not be separated from the observable peaks. All calibration sources and the nominal and visible energies of the  $\gamma$  lines are listed in Table 2.

Table 2: Radiation sources used for the energy calibration. For the  $\gamma$  lines, the nominal line energies and the visible line energies together with their resolutions calculated with the parameter of  $a = 30$  keV are listed. The two lines from  $^{60}\text{Co}$  are not resolved. For m.i.p.s, only the visible line energy from the GEANT4 simulation is available.

Radiation	Nominal Line	Visible Line
Source	Energy [MeV]	Energy [MeV]
$^{60}\text{Co}$	1.17/1.33	$1.02 \pm 0.17$
$\text{H}(\text{n}, \gamma)\text{D}$	2.2	$1.85 \pm 0.24$
$^{228}\text{Th}$	2.615	$2.31 \pm 0.26$
$^{241}\text{AmBe}$	4.438	$3.98 \pm 0.35$
m.i.p.s	—	$51.0 \pm 1.2$

The so-called pulse charges were calculated in ADC units by combining the integrated pulses of the two PMTs. The peaks in the resulting spectra were fitted to obtain the visible line energies in ADC units. These were calibrated against the visible line values obtained from equivalent fits to the simulated energy spectra, see Table 2. The resulting calibration points are shown in Fig. 4a, together with a fit of a third order polynomial function to these points. The result of this fit was used as the energy calibration function.

The calibrated data from the sources are shown together with the simulated spectra for  $^{60}\text{Co}$  and  $^{228}\text{Th}$  in Figs 4b and 4c respectively. The agreement is quite good.

The calibrated spectrum in the laboratory as measured with the Gd-LS detector is shown together with the simulated spectrum of energy deposited by cosmic muons and their secondary particles in Fig. 4d. The details of the simulation of cosmic muons passing through the overburden to the underground laboratory are discussed in Section 5. Both simulated and measured spectra are normalized to their corresponding lifetimes. The agreement is quite good above 4 MeV. The discrepancy below 4 MeV is due to environmental radioactivity which was not simulated.

For the event selection, a threshold of  $E_{thr} = 0.5$  MeV was set offline. Figure 4d shows that this was safely above the hardware threshold of the Gd-LS detector which was  $\approx 0.3$  MeV.

The energy calibration and threshold are based on the unit MeV. Neutron interactions deposit energies which are not as directly related to incident energies as is the case for  $\gamma$  or muon interactions. Therefore, from here on, the unit  $\text{MeV}_{ee}$ , where  $ee$  stands for electron equivalent, is used for neutron interactions, for which quenching is taken into account.

#### 4. Event Selection

The neutrons from muon-induced interactions are identified by signals recorded after the observation of a muon tag. The sample of events with the least background contamination are called nuclear recoil events.

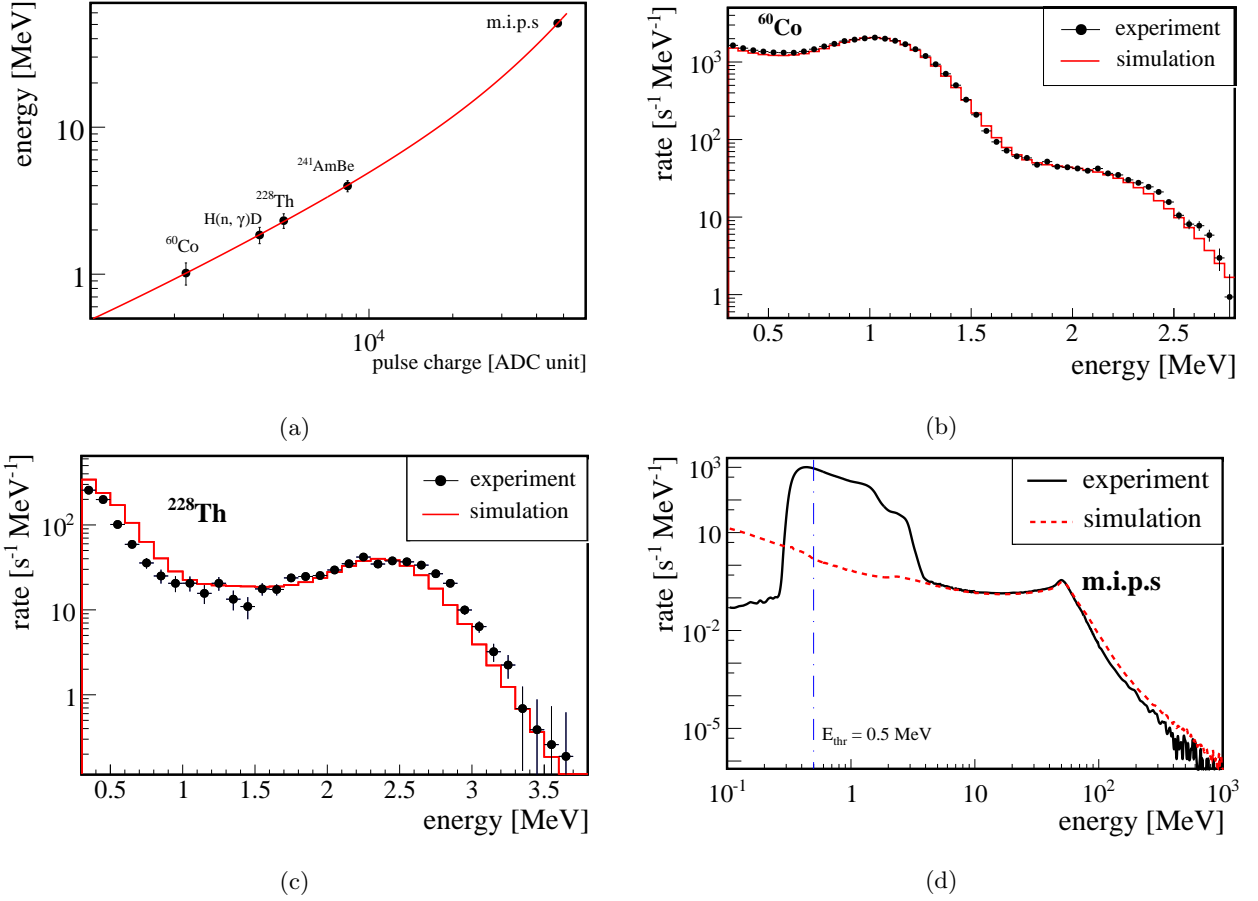


Fig. 4: Energy calibration. (a) Visible line energy versus so-called pulse charge as recorded for the PMTs as response to the sources listed in Table 2. The solid curve represents the result of a fit of a third-order polynomial to the points. The two lines from  $^{60}\text{Co}$  are not resolved. The error bars represent the resolutions calculated with the parameter  $a = 30\text{ keV}$ . This resolution parameter was used for all simulated distributions. Calibrated measured and simulated energy spectra for (b)  $^{60}\text{Co}$ , (c)  $^{228}\text{Th}$ . (d) Calibrated measured energy spectrum observed in the laboratory and predicted spectrum (GEANT4-9.6) of the energy deposited by cosmic muons and their secondary particles in the Gd-LS detector. The peak at 51 MeV is due to the passage of minimum ionizing particles. The simulated and the measured spectra are normalized to their corresponding lifetimes.



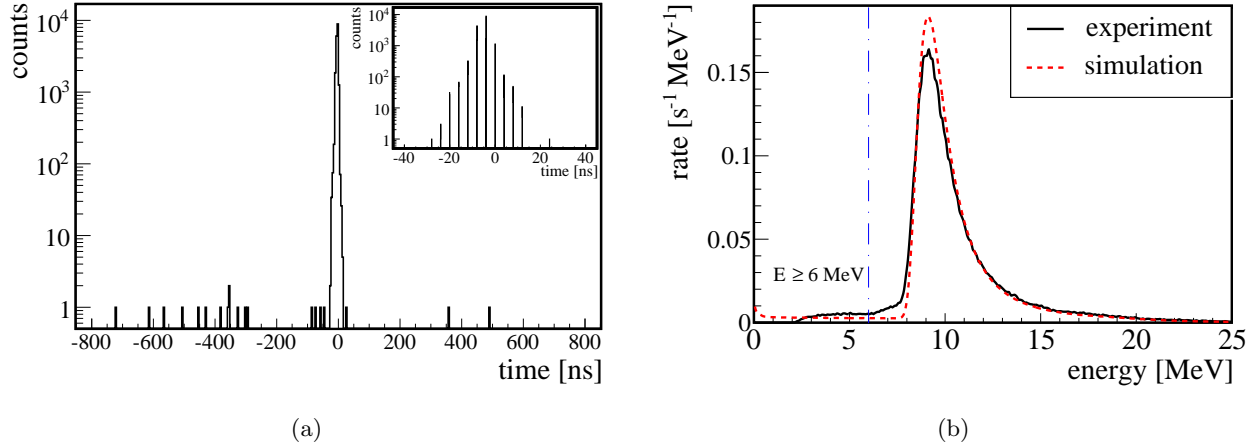


Fig. 5: Selection of muon tags. (a) Distribution of measured time differences for muon scintillator panel number 1 and number 4 for muon tags; the ADC sampling time is 4 ns, see insert. (b) Spectrum of the energy deposited in muon scintillator panel number 1 for muon tags. Also shown is the spectrum as predicted by simulation (GEANT4-9.6). The integral of the simulated spectrum was normalized to the integral of the measured spectrum.

They comprise three signals, a muon tag from the muon scintillator panels, a prompt signal from a nuclear recoil due to a neutron scattering off a nucleus in the Gd-LS detector, and a delayed  $\gamma$  signal from a neutron capture in the Gd-LS detector. The selection of these events demonstrates the capabilities of the detector best and therefore is described first.

A less restrictive and larger sample is composed of so called capture events, which are events with only a muon tag and a delayed capture signal. This sample contains also neutrons with energies too low to create a detectable nuclear recoil signal.

#### 4.1. Muon tagging

The passage of a muon through the right-side lead wall was tagged by coincident signals in the four muon scintillator panels (1, 2, 3, 4), see Fig. 3. The time difference between each pair of panels had to be below 30 ns. This was motivated by the measured time differences for 4-fold coincidences which are shown in Fig. 5a. The efficiency of this timing cut is 100% while the background for 4-fold coincidences can be neglected. The contribution of random coincidences was estimated from the single panel rates to be  $7 \times 10^{-6}$ . The passage of multiple muons and coincidences due to secondary particles were not discriminated against.

Figure 5b shows the distribution of the energy deposited in muon scintillator panel number 1 for such 4-fold coincidences; also shown is a corresponding simulation, see Section 5 for details. The integral of the simulated spectrum was normalized to the integral of the measured spectrum in order to compare the shapes. The peak in the spectrum, associated with the passage of minimum ionizing particles, was at  $\approx 10$  MeV.

The observed distributions for panels number 1 and 4 had a tail towards lower energies with a kink at 6 MeV. The simulated distributions also have a tail towards lower energies associated with muons which

only grazed either panel 1 or panel 4. However, the observed distributions indicate that the scintillator panels additionally had some inefficiencies for grazing muons. This caused entries in the shoulder above 6 MeV. Below 6 MeV, the observed distribution flattens out but this is already close to the threshold. Thus, for a muon tag, it was required that the energy deposited in all four scintillator panels was above 6 MeV. According to simulation, the requirement of this minimum energy for all four scintillator panels led to an efficiency of 94.6%.

The lifetime of the experiment was 151.6 days. In the data, 7.30 million muon tags were identified. The number of muon tags would have increased by 1.1%, if the energy cut would have been lowered to 5 MeV. It would have increased by 0.01%, if only a coincidence between muon scintillator panels 1 and 4 would have been required; this shows that the extra requirement to have signals in the large panels does not significantly diminish the efficiency for muons while reducing random coincidences to an insignificant level.

#### 4.2. Prompt signals in the Gd-LS detector as nuclear recoil candidates

The first signal in the Gd-LS detector following a muon tag in a predefined window was selected as a candidate for a signal from a nuclear recoil. As such a signal is expected to arrive on the scale of tens to hundreds of nanoseconds, it is called a prompt signal. The position of this time window was established according to simulation, see Section 5 for details, and according to delays due to the experimental setup.

The simulated distributions of the time,  $\Delta t_{\text{sig-}\mu}^{\text{sim}}$ , between a muon tag and a signal in the Gd-LS detector are shown in Fig. 6 for the individual contributions from muon-induced neutrons, muon-induced particles other than neutrons and secondary particles in muon-induced showers. The different origins of the particles led to different momentum distributions as different types of particles undergo different types of interactions on their paths from the right-side lead wall to the Gd-LS detector. As a result, the muon-induced neutrons take longer to reach the Gd-LS detector than other particles. As indicated in Fig. 6, the requirement of a time delay of 16 ns rejects most of the muon-induced non-neutron background, while maintaining a neutron detection efficiency of 97 %.

The delays due to the experimental setup,  $\Delta t_{\text{delay}}^{\text{exp}}$ , between the time of the interaction and the time at which the signal is recorded were due to the response time of the liquid scintillator of the Gd-LS detector,  $\Delta t_{\text{rsp}}$ , and the delay,  $\Delta t_{\text{cab}}$ , in the cables. The value of  $\Delta t_{\text{rsp}}$  for this type of Gd-LS detector was previously determined to be  $\approx 30$  ns, see Fig. 7. The delay in the cables was estimated to be  $\Delta t_{\text{cab}} \approx 14$  ns and the time resolution of the ADC was 4 ns. Thus,  $\Delta t_{\text{delay}}^{\text{exp}} = 48$  ns was estimated.

Accordingly, the search window for prompt signals was opened at a time difference,  $\Delta t_{\text{sig-}\mu} = 16 + \Delta t_{\text{delay}}^{\text{exp}} = 64$  ns, between the muon tag and the first signal in the Gd-LS detector with  $E \geq 0.5 \text{ MeV}_{ee}$ . The search window was closed at  $\Delta t_{\text{sig-}\mu} = 348$  ns. This maintained an efficiency of almost 100 %. If a second muon tag was found before the end of the window or a muon was identified in the left-side lead wall, the window was closed already at the respective time. As the total rate of identified muons in the right-side

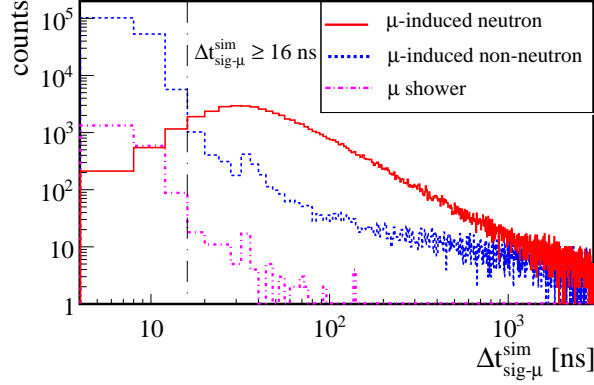


Fig. 6: Simulated (GEANT4-9.6) time between the first signal in the Gd-LS detector and a muon tag,  $\Delta t_{\text{sig-}\mu}^{\text{sim}}$ , for  $\mu$ -induced neutrons,  $\mu$ -induced other particles (non-neutrons) and secondary particles from showers induced by the muon before it entered the underground laboratory (shower).

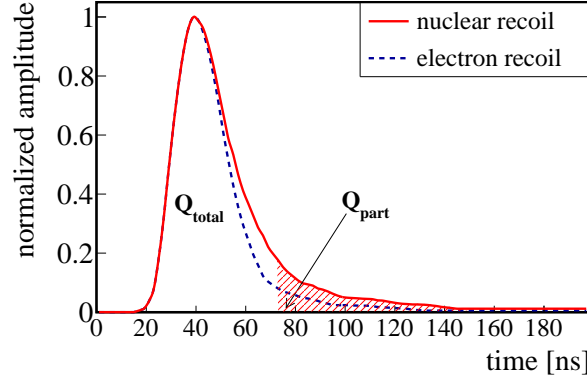


Fig. 7: Average waveform of neutron-induced nuclear recoil signals. Also shown are electron recoils induced by  $\gamma$ ,  $e^-$  or muon radiation. The data were obtained with an identical Gd-LS detector; plot taken from [29]. The parameter  $Q_{\text{total}}$  denotes the total integral of the waveform, while the  $Q_{\text{part}}$  denotes the integral of the tail of the waveform.

and left-side walls was only about 1 Hz, the probability for an early closure was below  $4 \times 10^{-7}$  and thus the efficiency was not affected.

A total of 15,494 prompt signals in the Gd-LS detector were selected as the candidates for nuclear recoils.

#### 4.3. Discrimination against signals from electron recoils

The sample of prompt signals still contains a considerable background from electron recoils due to  $\gamma$ , electron or muon interactions. The waveforms of the events in the Gd-LS detector can be used to distinguish between nuclear and electron recoil events. Figure 7 shows the average waveforms for nuclear and electron recoil events as obtained for an identical detector with an AmBe calibration measurement [29]. The tails of the waveforms are different. The parameter  $Q_{\text{total}}$  denotes the total integral of the waveform from 0 to

208 ns while  $Q_{part}$  denotes the integral from 76 ns to 208 ns. The observable  $Dis$

$$Dis = \frac{Q_{part_1} + Q_{part_2}}{Q_{total_1} + Q_{total_2}}, \quad (1)$$

where ‘1’ and ‘2’ stands for the two photo-multipliers of the Gd-LS detector, was constructed to distinguish between prompt signals from nuclear recoils and electron recoils.

#### 4.4. Delayed signal from $\gamma$ emission after neutron capture in the Gd doped liquid scintillator

A coincidence between a prompt signal and a delayed signal, presumably indicating a neutron capture, was also required to identify neutron-induced events. After thermalization, neutrons are captured in the Gd-LS after a diffusion time,  $\Delta t_{\gamma-n}$ . The diffusion time predominantly depends on the fraction of Gadolinium in the liquid scintillator, which is 0.5% for the liquid scintillator EJ-335 used in this experiment. The average value of  $\Delta t_{\gamma-n}$  of  $\approx 7 \mu\text{s}$  was determined with an AmBe neutron source, following the procedure developed for an identical Gd-LS detector [29].

To study the coincidences as observed in the data taken in the underground laboratory in Tübingen, preliminary cuts were used to select the nuclear recoils out of the prompt signals. A cut of  $Dis > 0.12$  was introduced and the energy of the prompt signal was limited to  $20 \text{ MeV}_{ee}$ . The distribution of the difference between the time of the nuclear recoil and the time of the delayed signal,  $\Delta t_{\gamma-n}$ , is shown in Fig. 8. Also shown are the predictions from two GEANT4 simulations, see Section 5. The predictions are normalized to the data in the time interval from 2 to  $40 \mu\text{s}$ . The shape of the measured distribution is quite well described. This shows that the preliminary selection of nuclear recoils is quite effective and that the predictions from simulation can be used to evaluate the efficiency of a  $\Delta t_{\gamma-n}$  cut.

The time window of  $2 \mu\text{s} < \Delta t_{\gamma-n} < 40 \mu\text{s}$  was chosen to select delayed  $\gamma$  signals from neutron capture. This rejected most of the accidental background while, according to simulation, retained an efficiency of  $\approx 84\%$ . The distribution of the energy deposited by the time-selected candidates for delayed  $\gamma$  signals is shown in Fig. 9. Again, the predictions from the GEANT4 simulations describe the data quite well. The  $\Delta t_{\gamma-n}$  selection was combined with the requirement that, the energy of the delayed signal was in the range of 0.5 to 9 MeV.

#### 4.5. Final selection of nuclear recoil events

Without the requirement that the energy recorded for the prompt signal was below  $20 \text{ MeV}_{ee}$  and preliminary  $Dis > 0.12$  cut, 4296 events within the time window from 2 to  $40 \mu\text{s}$  were selected. Figure 10 shows a scatter plot of the energy of the prompt signals versus  $Dis$  for these events. Also shown is the distribution of events from a calibration measurement with a  $^{228}\text{Th}$   $\gamma$ -source. The two distributions are not normalized to each other in any way. The events from the calibration data shown in Fig. 10 with an energy below  $4 \text{ MeV}_{ee}$  are predominantly due to  $\gamma$  rays from the  $^{228}\text{Th}$  source and form a clearly different class of

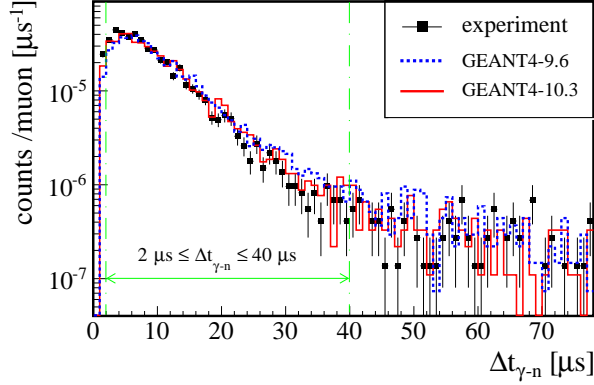


Fig. 8: The measured distribution of the time difference,  $\Delta t_{\gamma-n}$ , between candidate signals for  $\gamma$  rays emitted after neutron capture and the prompt signals identified as nuclear recoils through the cut  $Dis > 0.12$ . Also shown are two GEANT4 simulations, see Section 5, normalized to the integral of the measured distribution for  $2 \mu s < \Delta t_{\gamma-n} < 40 \mu s$ .

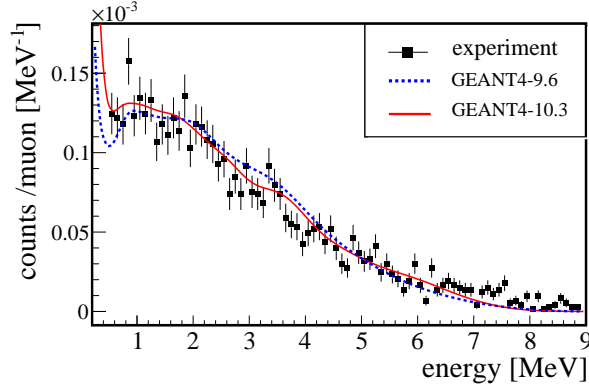


Fig. 9: The distribution of the energy observed for time-selected delayed signals following a prompt signal identified as a nuclear recoil by the cut  $Dis > 0.12$ . Also shown are predictions from two GEANT4 simulations which are normalized to the integral of the measured spectrum in the interval from 0.5 MeV to 9 MeV.

events. However, some events populate the nuclear recoil region. They are mainly due to environmental radioactivity. The events above  $4 \text{ MeV}_{ee}$  are due to cosmic radiation including muon-induced neutrons.

Below  $20 \text{ MeV}_{ee}$ , the two event classes are clearly separated. Above  $20 \text{ MeV}_{ee}$ , nuclear and electron recoils can not be distinguished efficiently because of changes in the waveforms. Thus, the requirement that the energy of the prompt signal was below  $20 \text{ MeV}_{ee}$  was retained. This reduces the sample by about 300 events.

For the final determination of the number of events, the usage of the  $Dis$  discriminator was refined. It was used in an energy-dependent way in order to discriminate as effectively as possible against electron recoils in the time-selected events with an energy of the prompt signal below  $20 \text{ MeV}_{ee}$ . An unbinned Maximum-Likelihood method was used to fit  $Dis$  with two Gaussian functions for each energy bin of  $0.5 \text{ MeV}_{ee}$  width. While the integral of the Gaussian with lower mean  $Dis$  is taken as the number of background events, the

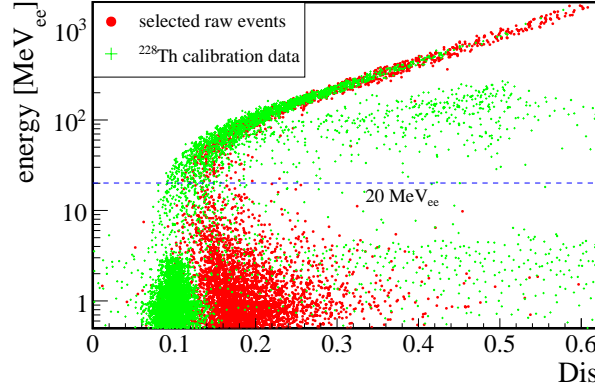


Fig. 10: Energy versus  $Dis$  discriminator for the prompt signals of time-selected events which are candidates for nuclear recoil signals. Also shown are events recorded for calibration data recorded with a  $^{228}\text{Th}$   $\gamma$ -source. The cut value for  $20 \text{ MeV}_{ee}$  is indicated by a horizontal dashed line.

integral with the higher mean  $Dis$  is taken as the number of events attributed to nuclear recoils. Figure 11a shows the mean and sigma values of the Gaussians from the fits. For some of the bins, the mean and sigma values are fluctuating due to a lack of statistics. This is taken into account through the uncertainties as given by the fits. Figure 11b depicts the fit results on the discriminator  $Dis$  for the typical energy bin from 2.5 to  $3.0 \text{ MeV}_{ee}$ . The good quality of the fit indicates that very few events with high  $Dis$  are lost.

In summary, nuclear recoil events were selected which comprised

- a muon tag indicating the passage of a muon through the right-side lead wall,
- followed by a prompt signal in the Gd-LS detector with an energy in the range of 0.5 to  $20 \text{ MeV}_{ee}$  and a time delay  $64 \text{ ns} < \Delta t_{\text{sig-}\mu} < 348 \text{ ns}$ ,
- followed by a delayed signal in the Gd-LS detector with an energy in the range of 0.5 to  $9 \text{ MeV}$  and a time delay  $2 \mu\text{s} < \Delta t_{\gamma-n} < 40 \mu\text{s}$ .

The final number of events was determined using fits to the  $Dis$  discriminator on the prompt signals in individual energy bins. The fits determined the number of background events to be  $457 \pm 35$ . The overall number of signal events was determined to be  $3534 \pm 68$ . The event numbers of nuclear recoils as determined from the fits were used for further analysis.

#### 4.6. Systematic uncertainties on the selection of nuclear recoil events

The systematic uncertainties had two main sources:

- changes in the energy scale;
- uncertainties due to the time resolution of the ADC.

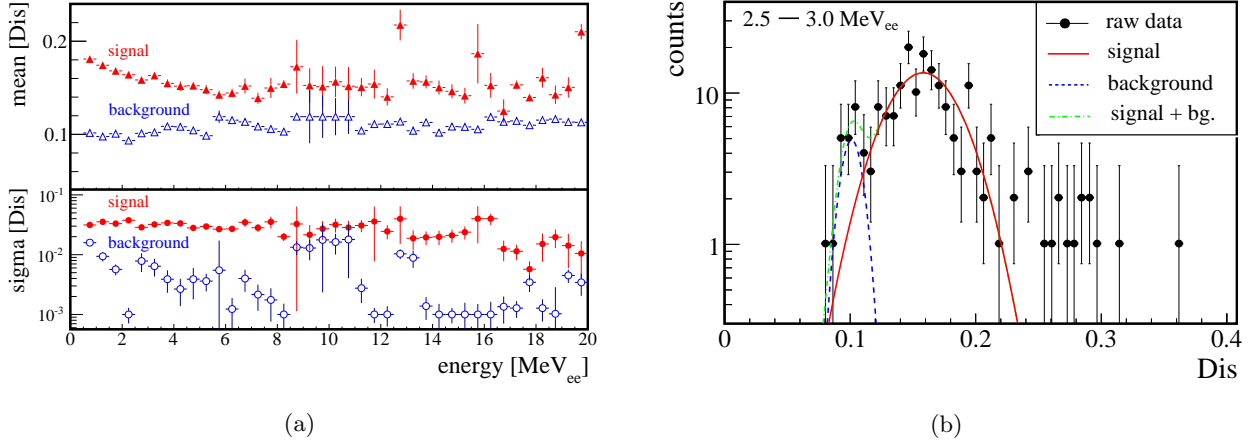


Fig. 11: Unbinned Maximum-Likelihood fit of two Gaussian functions to the  $Dis$  distributions. (a) The mean (top panel) and sigma (bottom panel) values of the Gaussians from the fits, both for signal and background; (b) Results of the Gaussian fit for the energy bin  $2.5 - 3.0 \text{ MeV}_{ee}$ ; the  $\chi^2/\text{dof}$  is 1.08 for this fit.

The energy scale as determined by the energy calibration, see Section 3, was not completely stable during the 5 months of data taking. The light yield of the liquid scintillator varied without a trend by 4.6 %. Folding in the energy resolution, the uncertainty on the energy scale was conservatively estimated to be  $\approx 10\%$ . When varying the offline threshold  $E_{thr} = 0.5 \text{ MeV}$  by 10 %, the number of signal events changes by 8.1 %.

The time resolution of the ADC affects the  $\Delta t_{\text{sig-}\mu}$  cut selecting prompt signals, see Section 4.2. When varying the  $\Delta t_{\text{sig-}\mu}$  cut by 4 ns, the number of signal events changes 7.5%. All other systematic uncertainties are negligible. The signal for nuclear recoil events with a delayed  $\gamma$  signal for a lifetime of 151.6 days becomes  $3534 \pm 68 \text{ (stat.)} \pm 390 \text{ (syst.)}$ .

#### 4.7. Selection of capture events

The requirement of an observable nuclear recoil excludes neutrons with low energies. Such neutrons are, however, abundantly produced in muon-induced interactions and they can be captured in the Gd-LS detector. The selected events comprise a muon tag and a delayed signal:

- a muon tag indicating the passage of a muon through the right-side lead wall,
- followed by a delayed signal in the Gd-LS detector with an energy in the range of  $E_{thr}^{\text{CE}} = 2.0$  to  $9 \text{ MeV}$  and a time delay  $2 \mu\text{s} < \Delta t_{\gamma-\mu} < 40 \mu\text{s}$ .

The observed  $\Delta t_{\gamma-\mu}$  distribution is shown in Fig. 12. Without the requirement of a coincident nuclear recoil, the background level is substantial. However, Fig. 12 demonstrates that signal events do not occur beyond  $\Delta t_{\gamma-\mu} = 40 \mu\text{s}$ . The accidental background was determined by fitting an exponential to the  $\Delta t_{\gamma-\mu} > 40 \mu\text{s}$  distribution. It was used to subtract the accidental background statistically.

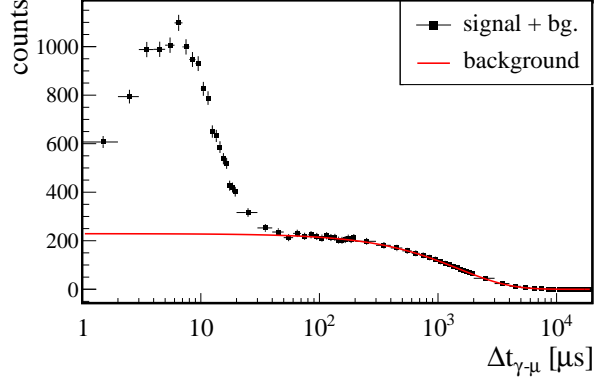


Fig. 12: The distribution of the time delay,  $\Delta t_{\gamma-\mu}$ , of the neutron capture signals with  $E_{thr}^{CE} = 2$  MeV with respect to the muon tags. The result of a fit of an exponential to the background for  $\Delta t_{\gamma-\mu} > 40 \mu s$  is shown as a solid line.

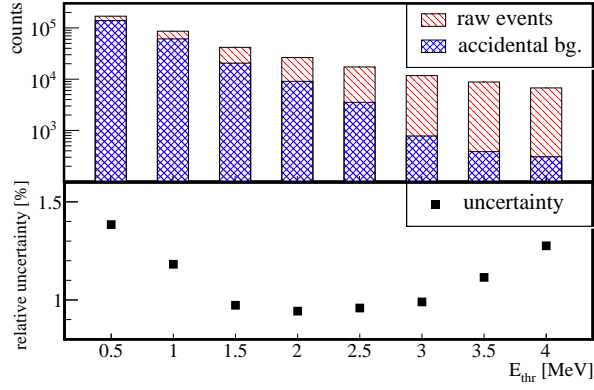


Fig. 13: Top panel: Raw number of selected capture events (raw events) and the contribution of accidental background (bg.) events as determined by exponential fits for different  $E_{thr}^{CE}$ . Bottom panel: Relative statistic uncertainties on the background subtracted event numbers.

The value of  $E_{thr}^{CE} = 2.0$  MeV was chosen to minimize the statistical uncertainty on the background subtracted event number. Figure 13 shows the raw number of selected neutron capture events and the number of accidental background events according to the fits as well as the resulting relative uncertainties depending on  $E_{thr}^{CE}$ . The uncertainty has a shallow, but distinct minimum at  $E_{thr}^{CE} = 2.0$  MeV.

For  $E_{thr}^{CE} = 2.0$  MeV, a total of  $26399 \pm 162$  events were selected including  $9082 \pm 21$  background events.

## 5. Monte Carlo

The MC simulation was performed in two stages:

1. propagation of muons from the surface to the underground lab;
2. muon interactions and physics in the experiment.



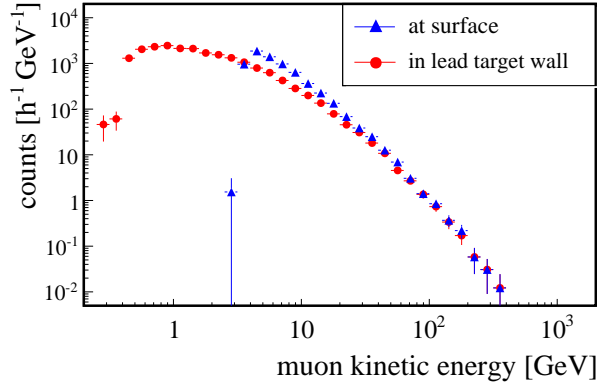


Fig. 14: Distribution of the kinetic energy of tagged muons at the surface and inside the lead wall simulated by FLUKA version 2011.2c. The latter was computed as the average of the kinetic energies above and below the wall.

For the first stage, FLUKA-2011.2c [30, 31] was used to simulate the propagation of cosmic muons through the overburden into the underground laboratory. The geometry was implemented according to the technical drawings where the material of the overburden was described as “densified soil”, for which a density of  $2.25 \text{ g/cm}^3$  was assumed. The average energy of the muons entering the laboratory from the top was found to be  $\approx 7 \text{ GeV}$ . The distributions of the kinetic energy of tagged muons at the surface and inside the lead wall are shown in Fig. 14. The average kinetic energy of tagged muons is  $11.2 \text{ GeV}$  on the surface and  $\approx 8 \text{ GeV}$  inside the lead wall.

The energy and angular distributions of cosmic muons above ground were parametrized [32]. A comparison to the world data on the muon momentum spectrum at sea-level available from the PDG [33] showed a good agreement in the region of interest. The underground laboratory is located at 452 meter above sea-level which causes a few percent increase of the muon flux as opposed to sea-level. In addition, low energy muons are subject to solar cycle, weather and seasonal atmospheric changes. Therefore, we assume a systematic uncertainty on the integral muon intensity of the order of 15%. However, the absolute flux is not important because all predictions are normalized to the number of observed muon tags.

A cross-check was performed starting the simulation from cosmic rays interacting in the earth atmosphere. A good agreement on energy and angular distributions in the laboratory was found. The mean energy of muons in the lab was confirmed within 5%. The angular distributions were also similar. The important quantity is the average path-length of  $51 \text{ cm}$  for tagged muons, which was confirmed within 2%.

The positions and momenta of the muons and their secondary particles on the surface of a virtual sphere with  $1 \text{ m}$  radius around the combined setup of MINIDEX and the Gd-LS detector were saved together with information on the relative time of arrival. This was the input to stage 2 of the simulation.

For the second stage, GEANT4 was used to simulate:

- the propagation of all muons and muon-induced secondary particles from the virtual sphere towards

MINIDEX,

- the production of muon-induced neutrons and the production of all other associated particles,
- the propagation of the neutrons and all other particles to the Gd-LS detector,
- the response of the Gd-LS detector.

The optical photon processes, i.e. the generation of scintillation light, light transportation and light collection, were not simulated. The energy depositions were taken as simulated by GEANT4. For nuclear recoils, the reduction of the light output due to quenching [34] was corrected for according to previous measurements for the Gd-LS type EJ-335 [35, 29].

Two versions of GEANT4 were used:

- GEANT4-9.6.p04 with the Shielding 2.0 modular physics list with the muon-nuclear reaction switched on by hand,
- GEANT4-10.3.p02 with the ShieldingM 2.1 modular physics list for which the muon-nuclear reaction is switched on by default.

The Shielding physics list was introduced for GEANT4-9.4. It was originally developed for studies related to ion-ion collisions and to the penetration power of neutrons. It is also suited to study aspects of neutron physics for underground and low background experiments. The Shielding physics list [36] contains a well motivated selection of simulation packages for electromagnetic and hadronic physics processes. Its high energy part is taken from the FTFP\_BERT [37] physics list. It uses FTFP and Bertini to simulate proton, neutron, pion and kaon interactions. For neutrons with an energy below 20 MeV, the list neutron\_HP [37] is used. The QMD model [38] is used to simulate the interactions of ions.

The ShieldingM physics list [39], which was developed for muon experiments, was introduced since GEANT4-10.1. It is based on the Shielding physics list with transition from the Bertini to the FTFP model happening in the region between 9.5 and 9.9 GeV.

The production threshold for protons in GEANT4-9.6 is by default 70 keV while in GEANT4-10.3 it is 0 keV to allow for low energy nuclear recoils. The threshold for secondary particle production is implemented as a distance cut in GEANT4. Specifically for this study, it was set to 0.1 mm in both GEANT4 versions. This corresponds to energy thresholds of  $\approx 30$  keV,  $\approx 240$  keV and  $\approx 230$  keV for  $\gamma$ ,  $e^-$  and  $e^+$  production in lead, and  $\approx 1$  keV and  $\approx 80$  keV for  $\gamma$  and  $e^-/e^+$  production in the Gd-LS. These values are well below the thresholds for  $\gamma$  and  $e^-/e^+$  nuclear reactions, and well below the Gd-LS detector energy threshold, see Section 3.

The dashed curve in Fig. 4d represents the spectrum of the energy deposited by cosmic muons and their secondary particles in the Gd-LS detector as predicted by GEANT4-9.6. The data are reasonably

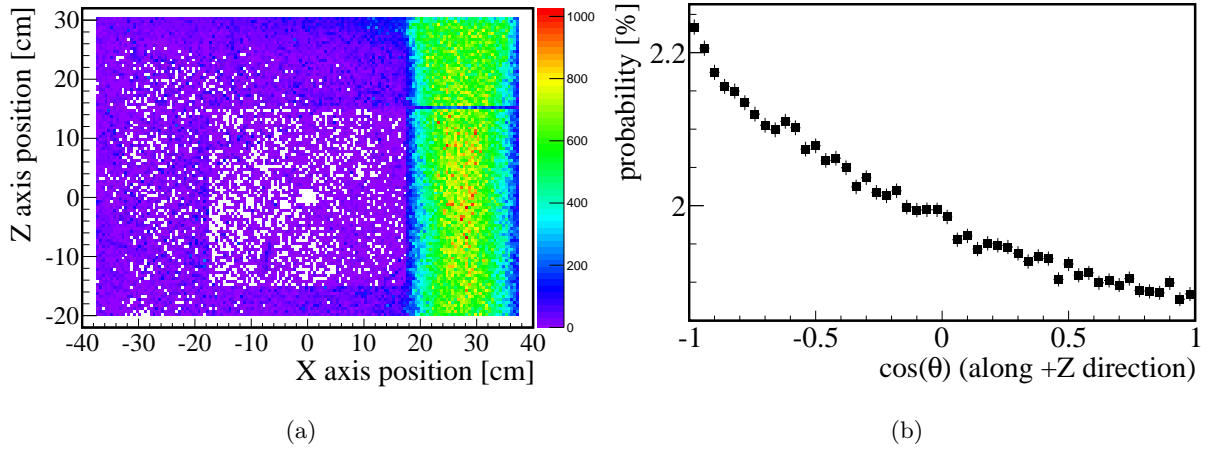


Fig. 15: Predicted (GEANT4-9.6) distributions of (a) the production position and (b) the azimuth angle of neutrons induced in lead in events with a muon tag, see Fig. 1 for the definition of the X and Z axis.

well described above an energy of 4 MeV, especially in the region of minimum ionizing particles. The discrepancy of the tail towards very high energies is due to saturation of the PMT readout and not modeled in simulation. This has, however, no influence on the experiment. Below 4 MeV, the data include events from natural radioactivity which was not part of the simulation.

The dashed curve in Fig. 5b represents the prediction for the spectrum of the energy deposited in muon scintillator panel 1 for events with a muon tag. The position of the peak and the tail towards higher energies are well described. The tail in the data toward lower energies is not described as no inefficiencies were simulated.

The number of simulated muon tags was  $\approx 28.7 \times 10^6$ . The average energy of the tagged muons was  $\approx 8$  GeV. The GEANT4-9.6 predicted distributions of the position of neutrons produced in events with a muon tag is shown in Fig. 15a. Here, only primary neutrons, i.e. neutrons produced directly by the tagged muons, and neutrons produced by muon-induced particles other than neutrons were considered. Secondary neutrons generated by primary neutrons were not considered. The production distribution follows the structure of the MINIDEX setup, see Section 2. Most of the neutrons are generated inside the right-side lead wall ( $17.5 \text{ cm} < X < 37.5 \text{ cm}$ ), which was used for tagging. The neutrons produced outside the right-side lead wall were generated by muon-induced particles such as  $\gamma$ , electrons, protons, pions and other particles.

The angular distribution of the neutrons is shown in Fig. 15b. The distribution shows that neutrons are predominantly produced downwards, but that this effect is not very strong. The number of upward going neutrons is predicted to be  $\approx 85\%$  of the number of downward going neutrons.

The predicted spectrum of the neutrons is shown in Fig. 16. Also shown are the individual contributions from the most important processes of neutron production. For energies above 2 MeV, the dominant process is indeed the production through muon-nuclear processes. However, there is substantial contribution from

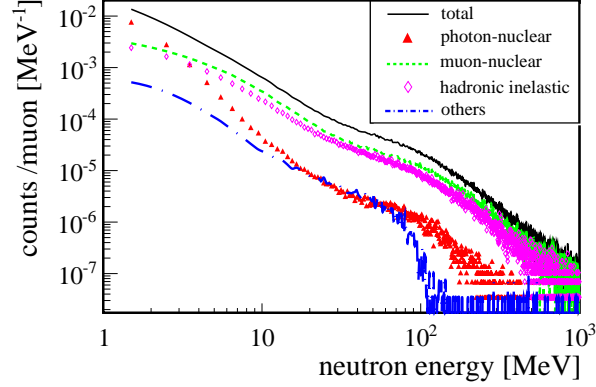


Fig. 16: The predicted (GEANT4-9.6) energy spectrum of neutrons produced in events with a muon tag. Also shown are the individual contributions from photon-nuclear, muon-nuclear, and hadronic-inelastic interactions. Other contributions include  $e^-/e^+$  nuclear reactions as well as  $\mu^-/\pi^-/K^-$  captures and decays.

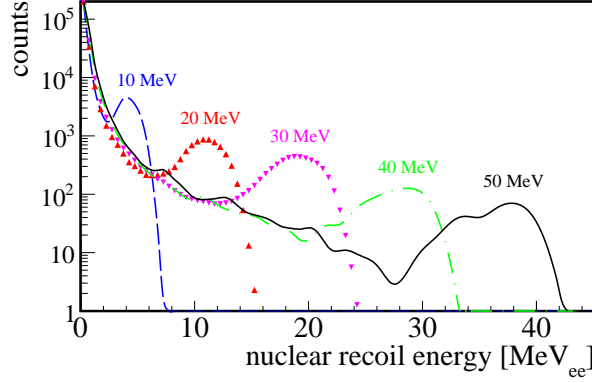


Fig. 17: Simulated (GEANT4-9.6) response functions of the Gd-LS detector for 10, 20, 30, 40 and 50 MeV mono-energetic neutrons homogeneously distributed in the lead. The signal quenching for nuclear recoils in the Gd-LS was included in the simulation.

hadronic inelastic scattering where the hadrons are created in a muon-induced shower.

The GEANT4 was also used to simulate the response of the Gd-LS detector to nuclear recoils. Figure 17 shows selected examples for mono-energetic neutrons with energies of 10, 20, 30, 40 and 50 MeV and production positions homogeneously distributed in the right-side lead wall with an isotropic angular distribution.

The time structure of the events as predicted by GEANT4 was already presented in Figs. 6 and 8. In Fig. 8, the predicted distribution of  $\Delta t_{\gamma-n}$ , the time between the prompt nuclear recoil and the capture signals, are compared to data. In the relevant time interval used for the selection, the normalized predicted distributions describe the data quite well. This confirms that the selection procedure is reasonable.

## 6. Results

The directly measured distributions related to the larger sample of capture events do not require further analysis and are, therefore, presented first. They can be directly compared to MC predictions. The nuclear recoil events were subject to further analysis which allowed the extraction of the neutron spectrum. The comparison of MC predictions to the result needs special consideration and is presented at the end.

### 6.1. Capture events

The time distribution of capture events was already shown in Fig. 12. After background subtraction, MC predictions normalized to the number of muon tags can be directly compared to the data. The result is shown in Fig. 18 for the predictions obtained with GEANT4-9.6 and GEANT4-10.3. The time development of the signal is quite well described. Contrary to this, the predicted overall signal strength is significantly too low for both MC versions. The relevant numbers are summarized in Table 3.

The only significant source of systematic uncertainty is the uncertainty on the energy scale of the Gd-LS detector of  $\approx 10\%$ . This translates to a systematic uncertainty of  $4.5\%$  on the number of events. After taking the systematic uncertainty into account, the factors by which the observation exceeds the predictions are  $1.65 \pm 0.02$  (stat.)  $\pm 0.07$  (syst.) and  $2.58 \pm 0.03$  (stat.)  $\pm 0.11$  (syst.) for GEANT4-9.6 and GEANT4-10.3, respectively.

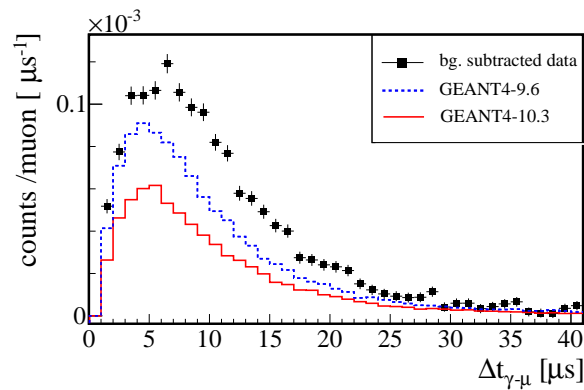


Fig. 18: The distributions of the time delay,  $\Delta t_{\gamma-\mu}$ , of the neutron capture signals with  $E_{thr}^{CE} = 2$  MeV with respect to the muon tags as observed and as predicted by GEANT4-9.6 and GEANT4-10.3. The distributions were normalized to the number of muon tags.

The excess factors for increasing  $E_{thr}^{CE}$  are listed in Table 4. The systematic uncertainty of  $4.5\%$  affects the factors in the same way for all values of  $E_{thr}^{CE}$ . Thus, only statistical uncertainties are considered. The discrepancy between observation and predictions increases with increasing energy threshold. This indicates that the spectrum of the delayed  $\gamma$  must be harder than predicted.

Table 3: Summary of observed and predicted event rates for all neutron capture events with an experimental energy threshold of  $E_{thr}^{CE} = 2$  MeV and for events with an identified nuclear recoil. The uncertainties for all muon capture events are statistical only.

	experiment	GEANT4-9.6 (Shielding)	GEANT4-10.3 (ShieldingM)
muon tags	$7.30 \times 10^6$	$28.72 \times 10^6$	$28.76 \times 10^6$
Neutron capture events	$26399 \pm 162$	$41309 \pm 203$	$26406 \pm 162$
Background	$9082 \pm 21$	–	–
Background subtracted events ( $\times 10^3$ )	$17.32 \pm 0.16$	$41.31 \pm 0.20$	$26.41 \pm 0.16$
Neutron captures per muon tag ( $\times 10^{-3}$ )	$2.37 \pm 0.02$	$1.438 \pm 0.007$	$0.918 \pm 0.006$
Ratio observation/MC	–	$1.65 \pm 0.02$	$2.58 \pm 0.03$
Nuclear Recoil Events	$3534 \pm 68$	$6255 \pm 79$	$3703 \pm 61$
Events per muon tag ( $\times 10^{-4}$ )	$4.84 \pm 0.09$	$2.18 \pm 0.03$	$1.29 \pm 0.02$
Systematic uncertainty	11%	–	–
Ratio observation/MC	–	$2.22 \pm 0.05(\text{stat.})$ $\pm 0.25(\text{syst.})$	$3.76 \pm 0.09(\text{stat.})$ $\pm 0.41(\text{syst.})$

Table 4: Ratios of observed over predicted rates for neutron capture events depending on the experimental energy threshold  $E_{thr}^{CE}$ . Uncertainties are statistical only.

$E_{thr}^{CE}$	GEANT4-9.6	GEANT4-10.3
0.5 MeV	$1.71 \pm 0.02$	$2.60 \pm 0.04$
1.0 MeV	$1.64 \pm 0.02$	$2.53 \pm 0.03$
1.5 MeV	$1.64 \pm 0.02$	$2.57 \pm 0.03$
2.0 MeV	$1.65 \pm 0.02$	$2.58 \pm 0.03$
2.5 MeV	$1.67 \pm 0.02$	$2.58 \pm 0.03$
3.0 MeV	$1.74 \pm 0.02$	$2.64 \pm 0.03$
3.5 MeV	$1.87 \pm 0.03$	$2.71 \pm 0.04$
4.0 MeV	$2.11 \pm 0.03$	$3.04 \pm 0.05$
4.5 MeV	$2.34 \pm 0.04$	$3.23 \pm 0.06$

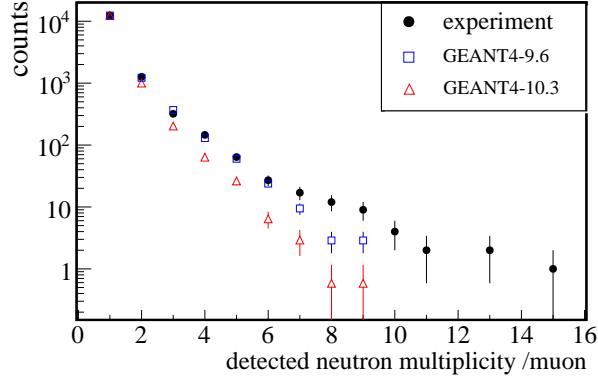


Fig. 19: The distribution of multiplicities for neutron capture signals with  $E_{thr}^{CE} = 2$  MeV as observed and predicted by GEANT4-9.6 and GEANT4-10.3. The predictions were normalized by normalizing the predicted number of events with multiplicity one to the observed number of events with multiplicity one.

The majority of the capture events, 71 %, have exactly one signal indicating neutron capture. However, there are events with more than one delayed  $\gamma$  in the time window  $2\mu\text{s} < \Delta t_{\gamma-\mu} < 40\mu\text{s}$ . This indicates that more than one neutron was produced, reached the Gd-LS detector and was captured. The distributions of detected multiplicities of neutron capture signals in events with one muon tag are shown in Fig. 19 as measured and as predicted by the two GEANT4 versions. The predictions were normalized by normalizing the predicted number of events with multiplicity one to the background subtracted observed number of events with multiplicity one. GEANT4-9.6 does better than GEANT4-10.3, which significantly underestimates the number of high multiplicity events.

## 6.2. Nuclear recoil events

The selection and treatment of events, in which in addition to the capture signal also a signal indicating a prompt nuclear recoil was identified, was described in detail in Section 4. The resulting nuclear recoil spectrum normalized to the number of muon tags is shown in Fig. 20, obtained from the double-Gaussian fits described in Section 4.5. Also shown in Fig. 20 are the predictions of the two MC versions. As for all capture events, the predictions are significantly below the number of observed nuclear recoils. In the energy range of  $0.5 - 20$  MeV<sub>ee</sub>, the integrated number of predicted events is a factor of  $2.22 \pm 0.05$  (stat.)  $\pm 0.24$  (syst.) too low for GEANT4-9.6. For GEANT4-10.3, the factor is  $3.76 \pm 0.09$  (stat.)  $\pm 0.41$  (syst.). The relevant numbers are listed in Table 3.

The deficit in the GEANT4 predictions for this subset of the neutron events is larger than for the complete neutron capture data set. As the identification of a nuclear recoil requires a neutron energy of at least about 5 MeV, this already suggests that the neutron spectrum is harder than predicted.

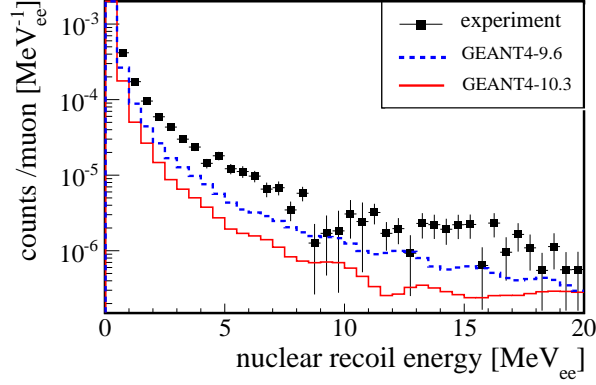


Fig. 20: Spectra of nuclear recoils as extracted for events with capture and nuclear recoil signals as measured and predicted. The signal quenching for nuclear recoils in the Gd-LS was part of the simulations. All spectra were normalized to the respective number of muon tags. Only the statistical uncertainties of the measurement are shown.

### 6.3. Neutron spectrum

Due to the basically background free determination of the nuclear recoil spectrum, it was possible to actually measure the neutron spectrum by unfolding the nuclear recoil spectrum. To do so, the energy dependent response functions of the Gd-LS detector were determined by GEANT4 simulation as demonstrated in Fig. 17 for mono-energetic neutrons produced homogeneously inside the right-side wall. The simulation was performed for neutron energies from 1 to 50 MeV in 0.5 MeV steps.

The simulated response functions were used as input to the iterative unfolding method SAND-II [40]. A vector  $\Phi_i^J$  with  $i$  indicating the energy bin ( $i = 1, \dots, I$ ) and width  $\Delta E_i$  is the result of the procedure after  $J$  iterations;  $\Phi_i^j$  represents the result after  $j$  iterations. Each iteration is performed as:

$$\Phi_i^{j+1} = \Phi_i^j \exp \left( \frac{\sum_{k=1}^K W_{ik}^j \ln(U_k^j)}{\sum_{k=1}^K W_{ik}^j} \right) \quad (2)$$

for  $j = 0, 1, \dots, J$

with

$$W_{ik}^j = \frac{R_{ki} \Phi_i^j}{\sum_{i=1}^I R_{ki} \Phi_i^j} \frac{N_k^2}{\sigma_k^2}, \quad U_k^j = \frac{N_k}{\sum_{i=1}^I R_{ki} \Phi_i^j \Delta E_i}$$

where  $K$  is the number of bins of the nuclear recoil spectrum;  $R_{ki}$  is the response function at the  $k^{th}$  bin for the  $i^{th}$  energy of mono-energetic neutrons;  $N_k$  is the measured number of nuclear recoils for the  $k^{th}$  bin with the uncertainty  $\sigma_k$ . A flat spectrum  $\Phi_i^0$  was chosen to start the iteration. The number of iterations  $J$ , after which the procedure ends, is determined with convergence monitoring.

The method was previously confirmed through the unfolding of a spectrum from an AmBe neutron source using a similar detector with the same dimensions and filled with identical Gd-LS [29].



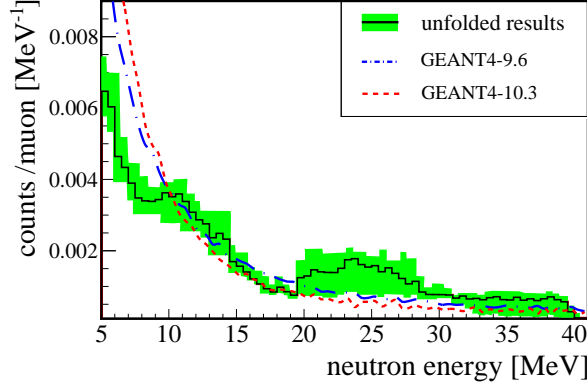


Fig. 21: The unfolded spectrum of neutrons induced by muons in lead (solid histogram). The band corresponds to the total uncertainties, see text for details. Also shown are the predictions obtained with GEANT4-9.6 and GEANT4-10.3 normalized to the area of the unfolded spectrum from 5 MeV to 40 MeV.

The result of the unfolding procedure is the neutron spectrum shown in Fig. 21. In order to estimate the combined statistical and systematic uncertainties, the unfolding was repeated with

- response functions obtained for the simulated position and angular distributions as shown in Fig. 15;
- a variation of the experimental energy scale of  $\pm 10\%$ ;
- The  $N_k$  values varying by their statistical uncertainties.

The band in Fig. 21 represents the envelope of all resulting changes to the spectrum. Also shown in Fig. 21 are the predictions from the GEANT4 simulations using the versions 9.6 and 10.3. The simulated spectra were normalized to the area of the measured spectrum in the energy range from 5 MeV to 40 MeV in order to compare the spectral shapes. Even though the uncertainties are significant, the observed spectrum is clearly harder than the predicted spectra. This is more pronounced for GEANT4-10.3

As a consistency check, the unfolded neutron spectrum was used as the input to GEANT4-9.6 to obtain the nuclear recoil spectrum. The uncertainties as listed above were again considered by using the respective neutron spectra as inputs. The resulting band of predictions is compared to the measurement in Fig. 22a. The measured nuclear recoil spectrum is reproduced very well above  $1 \text{ MeV}_{ee}$ .

The energy spectrum of the neutrons also influences the distribution of the time difference  $\Delta t_{\text{sig-}\mu}$  between the muon tag and the nuclear recoil signal. The unfolded neutron spectrum and its uncertainties were again used as input to GEANT4-9.6 to simulate the corresponding  $\Delta t_{\text{sig-}\mu}$  distribution. The result is shown in Fig. 22b together with the measured distribution and the distributions predicted by the two GEANT4 versions. All three simulated time distributions were shifted by  $+48 \text{ ns}$  to account for the experimental time delay  $\Delta t_{\text{delay}}^{\text{exp}}$ , see Section 4.2.

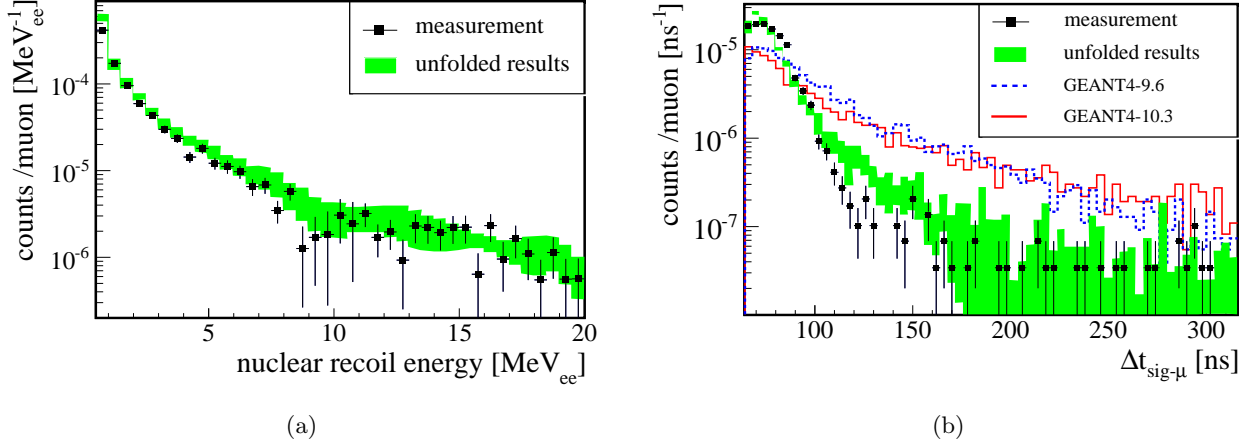


Fig. 22: (a) Nuclear recoil spectrum as observed and as reproduced by GEANT4-9.6 from the unfolded neutron spectrum as shown in Fig. 21. (b) Distribution of the time delay between muon tag and neutron nuclear recoil signal as observed, as reproduced by GEANT4-9.6 from the unfolded neutron spectrum and as predicted by GEANT4-9.6 and GEANT4-10.3. The bands represent the uncertainties due to the uncertainties on the measured neutron spectrum used as input to the MC, see text for details.

The prediction resulting from the unfolded neutron spectrum describes the data reasonably well. This demonstrates the consistency of the unfolded neutron spectrum and the measured  $\Delta t_{\text{sig-}\mu}$  distribution. It also confirms that the estimate of  $\Delta t_{\text{delay}}^{\text{exp}} = 48 \text{ ns}$  is realistic. The  $\Delta t_{\text{sig-}\mu}$  distributions as predicted by the two GEANT4 versions do not describe the data. As GEANT4-9.6 describes the data quite well with the unfolded neutron spectrum as input, the discrepancy can be attributed to the predicted neutron spectrum and not to problems in the simulation of neutron transport.

## 7. Discussion on GEANT4 performance

The number of observed neutron captures and neutron nuclear recoils is significantly higher than predicted by the two GEANT4 versions. In addition, the predicted neutron spectrum is too soft. Comparing the performance of the two GEANT4 versions it is observed that not only the overall deficit of neutrons is even higher for the newer version GEANT4-10.3, but also the neutron spectrum is even softer, see Fig. 21. The deficit in predicted high-multiplicity events is also larger for GEANT4-10.3, see Fig. 19.

The overall deficits cannot be explained without a considerable deficit in neutrons produced in muon-nucleon interactions. In addition, the problems with the angular distribution of muon-induced neutrons in GEANT4 as observed by NA55 [23] might contribute.

The deficit in the prediction of high multiplicity events, see Fig. 19, especially pronounced for GEANT4-10.3, could be due to primary production or due to a deficit in secondary neutron production. Probably, the corresponding physics processes affect both. The softness of the predicted neutron spectra could also

cause a deficit in secondary particle production. The lack of predicted high-multiplicity events confirms the overall weaker performance of GEANT4-10.3.

The softness of the predicted neutron spectra has to be linked to the implementation of the physics processes relevant for muon-induced neutron production. This is confirmed in that the time structure of nuclear recoil events can only be reproduced if the measured spectrum is used in the Monte Carlo, see Fig. 22b.

The observation of a harder than predicted neutron spectrum is significant, even though the measured nuclear recoil spectrum see Fig. 20, from which it is unfolded, does not have high-energy information due to the selection cut of  $20 \text{ MeV}_{ee}$ . This limitation has to influence the high-energy part of the unfolded neutron spectrum somewhat. However, as the usage of the unfolded neutron spectrum in GEANT4 reproduces the time structure of the observed nuclear recoil events, the influence has to be small, at least in the neutron energy range of  $5 - 40 \text{ MeV}$ .

The results presented here can hopefully help to improve the GEANT4 simulations. The excess in observed rates cannot be used to scale predictions for deep underground laboratories because the muon spectra there are shifted towards significantly higher energies. The measurements cannot be repeated at such deep depths because of a lack of muon rate. Thus, the physics process have to be better understood to make reliable predictions.

## 8. Summary and conclusions

Neutrons induced by cosmic muons in lead were studied in detail with a Gadolinium doped liquid scintillator detector which was installed in the shallow underground laboratory operated by the University of Tübingen, next to the Muon-Induced Neutron Indirect Detection EXperiment. The MINIDEX plastic scintillators were used for muon tagging. Samples of events with a neutron capture signal and with a prompt nuclear recoil signal and a neutron capture signal were established with high statistical significance.

Predictions made with the GEANT4 versions 9.6 and 10.3 were compared to the data. For neutron capture events, the observation exceeds the predictions by factors of  $1.65 \pm 0.02 \text{ (stat.)} \pm 0.07 \text{ (syst.)}$  and  $2.58 \pm 0.03 \text{ (stat.)} \pm 0.11 \text{ (syst.)}$  for GEANT4-9.6 and GEANT4-10.3, respectively. For neutron nuclear recoil events, which require neutron energies above approximately  $5 \text{ MeV}$ , the factors are even larger,  $2.22 \pm 0.05 \text{ (stat.)} \pm 0.25 \text{ (syst.)}$  and  $3.76 \pm 0.09 \text{ (stat.)} \pm 0.41 \text{ (syst.)}$ , respectively.

The multiplicity of neutron captures per muon was investigated. Events with multiplicity as high as 15 were observed. Neither GEANT4 version predicts events with such high multiplicities. Version 9.6 does quite well up to multiplicities of 6 while version 10.3 already fails at a multiplicity of 3.

The energy spectrum of nuclear recoils was also observed with high precision for recoil energies up to  $20 \text{ MeV}_{ee}$ . This recoil spectrum was used to obtain the spectrum of neutrons in lead by unfolding. This

represents the first statistically significant measurement of the spectrum of neutrons induced by cosmic muons in lead in a shallow underground laboratory.

The observed spectrum is harder than the spectra predicted by the two GEANT4 versions. The time structure of the nuclear recoil events is not described by the MC as is. However, if the observed spectrum is used as an input, the time structure is reasonably well described. This indicates that the problems with the GEANT4 description of the data arise from problems with the implementation of the processes contributing to the creation of neutrons and not with neutron transport. The hope is that the results presented here on the rate of neutron production and on the neutron spectrum can help to improve the GEANT4 simulations.

## Acknowledgments

This work was supported by the China Scholarship Council (CSC) (Contract No. 201606240105) and the Max-Planck-Society.

## References

## References

- [1] M. Agostini et al. (GERDA Collaboration), [Nature](#) **544** (2017) 47-52.
- [2] C. Patrignani et al. (Particle Data Group), [Chin. Phys. C](#) **40** (2016) 100001.
- [3] J. L. Liu et al., [Nat. Phys.](#) **13** (2017) 212216.
- [4] Q. R. Ahmad et al. (SNO Collaboration), [Phys. Rev. Lett.](#) **87** (2001) 071301; S. Fukuda et al. (Super-Kamiokande Collaboration), [Phys. Rev. Lett.](#) **86** (2001) 5656; F. P. An et al. (Daya Bay Collaboration), [Phys. Rev. Lett.](#) **108** (2012) 171803.
- [5] W. Xu et al. (Majorana Collaboration), [J. Phys. Conf. Ser.](#) **606**(1) (2015) 012004.
- [6] K. J. Kang et al., [Front. Phys.](#) **8** (2013) 412; W. Zhao et al. (CDEX Collaboration), [Phys. Rev. D](#) **93** (2016) 092003; S.K. Liu et al. (CDEX Collaboration), [Phys. Rev. D](#) **95** (2017) 052006.
- [7] C. Wiesinger, L. Pandola and S. Schnert, [arXiv:1802.05040\[hep-ex\]](#)
- [8] H. M. Araújo et al., [Astroparticle Physics](#) **29** (2008) 471481.
- [9] H. M. Kluck, Measurement of the cosmic-induced neutron yield at the Modane underground laboratory, PhD Thesis KIT, Karlsruhe (2013). DOI: [10.1007/978-3-319-18527-9](#).
- [10] G. V. Gorshkov, V. A. Zhabkin, and R. M. Yakovlev, Trans. by J. G. Adashko, [Sov. J. Nucl. Phys](#) **18.1** (1974) 5761, Orig. pub. as [Yad. Fiz.](#) **18** (1973) 109117 [in Russian].
- [11] I. Abt et al., [Astropart. Phys.](#) **90**, 1 (2017). DOI: [10.1016/j.astropartphys.2017.01.011](#)
- [12] M. F. Crouch and R. D. Sard, [Phys. Rev.](#), 2nd ser., **85.1** (1952) 120129. DOI: [10.1103/PhysRev.85.120](#).
- [13] M. Annis et al., [Phys. Rev.](#) **94**, 4 (1954). DOI: [10.1103/PhysRev.94.1038](#).
- [14] G. V. Gorshkov, V. A. Zhabkin, and R. . Yakovlev, Trans. by C. S. Robinson, [Sov. J. Nucl. Phys.](#) **13.4** (1971) 450452, Orig. pub. as [Yad. Fiz.](#) **13** (1971) 791796 [in Russian].
- [15] A. M. Short, In Proceedings of the 9th International Cosmic Ray Conference, (London, UK), 1 (1965) 10091011. ADS: [1965IC RC....2.1009S](#).
- [16] L. Bergamasco, [Nuovo Cim. B](#) **66.1** (1970) 120128. DOI: [10.1007/BF02710194](#).

- [17] G. V. Gorshkov and V. A. Zyabkin, Trans. by J. G. Adashko, Sov. J. Nucl. Phys. 7.4 (1968) 470474, Orig. pub. as Yad. Fiz. 7 (1968) 770777 [in Russian].
- [18] G. V. Gorshkov and V. A. Zyabkin, Trans. by J. G. Adashko, Sov. J. Nucl. Phys. 12.2 (1971) 187190, Orig. pub. as Yad. Fiz. 12 (1970), 340346 [in Russian].
- [19] L. Reichhart et al., [Astroparticle Physics 47 \(2013\) 6776](#).
- [20] L. Bergamasco, S. Costa, and P. Picchi, Nuovo Cimento A 13 (1973) 403412. DOI: [10.1007/BF02827344](#).
- [21] M. R. Adams et al. [E665 Collaboration], Phys. Rev. Lett. 74 (1995) 5198. DOI: [10.1103/PhysRevLett.80.2020](#).
- [22] V. Chazal et al., Nucl. Instrum. Meth. A 490 (2002) 334343. DOI: [10.1016/S0168-9002\(02\)01006-9](#).
- [23] M. G. Marino et al, Nucl. Instrum. Meth. A 582 (2007) 611620. DOI: [10.1016/j.nima.2007.08.170](#).
- [24] Y. Nakajima et al, AIP Conference Proceedings 1672, 090002 (2015). DOI: [10.1063/1.4928000](#).
- [25] P. Grabmaier, Universität Tübingen, private communication.
- [26] [www.eljentechnology.com/products/liquid-scintillators/ej-331-ej-335](http://www.eljentechnology.com/products/liquid-scintillators/ej-331-ej-335).
- [27] <http://geant4.cern.ch>
- [28] E. Tziaferi et al., [Astropart. Phys. 27 \(2007\) 326](#).
- [29] Q. Du et al, [Nucl. Instrum. Meth. A 889 \(2018\) 105112](#).
- [30] T. T. Boehlen et al., [Nuclear Data Sheets 120 \(2014\) 211-214](#).
- [31] A. Fassò et al., CERN-2005-10, INFN/TC-05/11, SLAC-R-773 (2005).
- [32] L. N. Bogdanova et al., [Phys. Atom. Nucl 69 \(2006\) 1293-1298](#). arXiv:nucl-ex/0601019
- [33] K. A. Olive et al. (Particle Data Group), [Chin. Phys. C 38 \(2014\) 090001](#).
- [34] J. B. Birks, *The Theory and Practice of Scintillation Counting*, Pergamon, New York, (1964).
- [35] Q. Du et al., [JINST 13 \(2018\) P04001](#).
- [36] GEANT4 Collaboration, [Shielding Physics List: for shielding, underground and high energy applications; Shielding Physics List Description](#)
- [37] [GEANT4 Reference Physics Lists](#)
- [38] GEANT4 Collaboration, [GEANT4 9.4 Release Notes](#); [GEANT4 9.5 Release Notes](#); [GEANT4 9.6 Release Notes](#).
- [39] M. Asai et al. (GEANT4 Collaboration), [The GEANT4 Version 10 Series](#).
- [40] S. L. Wang et al., [Chin. Phys. C 33 \(2009\) 378](#); W. N. McElroy et al., U.S. Air Force Weapons Laboratory Report AFWL-TR-67-41 (1967); H. Sekimoto and N. Yamamuro, Nucl. Sci. Eng. 80 (1982) 101; J. T. Routti and J. V. Sandberg, Rad. Prot. Dosim. 10 (1985) 103.